Research Square

Preprints are preliminary reports that have not undergone peer review.
They should not be considered conclusive, used to inform clinical practice,
or referenced by the media as validated information.

Effect of cooling conditions on microstructure evolution and tensile deformation behavior of friction stir welded NiCoCr medium-entropy alloy

Borui Zhang
Nanjing University of Aeronautics and Astronautics College of Material Science & Technology
Jinpeng Hu
Nanjing University of Aeronautics and Astronautics College of Material Science & Technology
Zhikang Shen
Southwest University College of Engineering and Technology
Tzuhsiu Chou
City University of Hong Kong
Yifu Shen
shenyifu0501@gmail.com
Nanjing University of Aeronautics and Astronautics College of Material Science & Technology
https://orcid.org/0000-0002-7162-262X
Guoqiang Huang
Nanjing University of Aeronautics and Astronautics College of Material Science & Technology

Research Article

Keywords: NiCoCr medium-entropy alloy, Friction stir welding, Cooling conditions, Dynamic recrystallization, Strain partitioning, Tensile properties

Posted Date: November 19th, 2026

DOI: https://doi.org/10.21203/rs.3.rs-11608750/v1

License: This work is licensed under a Creative Commons Attribution 4.0 International License.
Read Full License

Effect of cooling conditions on microstructure evolution and tensile deformation behavior of friction stir welded NiCoCr medium-entropy alloy

Borui Zhang [a], Jinpeng Hu [a], Zhikang Shen[b],Tzuhsiu Chou[c,*], Yifu Shen [a],Guoqiang Huang [a,*]
[a] College of Materials Science and Technology, Nanjing University of Aeronautics and Astronautics, Nanjing 210016, China
[b]College of Engineering and Technology, Southwest University, Chongqing, 400715, China
[c]Department of Materials Science and Engineering, City University of Hong Kong, Hong Kong, China

Abstract

The influence of cooling conditions on the microstructure and transverse tensile behavior of friction stir welded NiCoCr medium-entropy alloy was investigated by comparing air-cooled friction stir welding (AFSW) with alcohol–dry ice-assisted friction stir welding (LFSW) under identical nominal welding parameters. Both conditions produced sound joints containing fine, predominantly equiaxed grains in the nugget zone (NZ). Compared with AFSW, LFSW reduced the average grain size from 4.85 to 3.75 μm in the upper NZ and from 4.77 to 3.93 μm in the lower NZ. The finer-grained LFSW joint exhibited a higher yield strength (546 ± 3 MPa) than AFSW (471 ± 3 MPa), while their ultimate tensile strengths remained comparable (828 ± 7 and 836 ± 4 MPa, respectively). In contrast, uniform elongation decreased from 62.9 ± 5% for AFSW to 25.0 ± 2% for LFSW. Electron backscatter diffraction revealed progressive grain subdivision and recrystallization across the base material–thermo-mechanically affected zone–NZ transition in both joints. Digital image correlation further showed that plastic strain was preferentially accommodated outside the refined NZ, with more pronounced spatial strain partitioning in the LFSW joint. These results demonstrate that intensified external cooling promotes NZ grain refinement and increases joint yield strength, but its benefit is offset by reduced deformation compatibility during transverse tension. The comparison establishes the importance of balancing local NZ strengthening with strain accommodation across the entire welded joint.

Keywords: NiCoCr medium-entropy alloy; Friction stir welding; Cooling conditions; Dynamic recrystallization; Strain partitioning; Tensile properties

1 Introduction

Equiatomic NiCoCr (CrCoNi) medium-entropy alloy (MEA) has attracted considerable interest as a face-centered cubic (FCC) structural alloy because of its substantial work-hardening capacity and excellent fracture resistance, particularly at low testing temperatures [1,2]. Its yield strength can be increased through grain refinement, with grain boundaries and annealing twins contributing to the mechanical response [3,4]. For components produced from microstructurally tailored alloys, however, the capability to retain favorable properties after joining is also essential. Welding changes the original grain structure locally and produces distinct microstructural regions across a joint. Consequently, both the strength of the weld region and the distribution of plastic deformation across the joint need to be considered. Laser welding has been successfully applied to NiCoCr MEAs [5], whereas solid-state joining offers a means of avoiding the solidification microstructures associated with fusion welding.

Friction stir welding (FSW) combines severe plastic deformation with frictional heating and dynamic recrystallization, making it an effective approach for microstructural modification and joining of metallic materials [6,7]. FSW of CoCrNi MEAs has been shown to refine the stir-zone grains and increase their local resistance to deformation [8]. Our previous investigation of submerged FSW of fine-grained NiCoCr demonstrated that cooling-assisted joining can retain a favorable strength–ductility combination [9]. Thermal management is therefore an important variable in FSW, since the extent of heat extraction affects the final grain

*Corresponding author.

E-mail address: gqhuang@nuaa.edu.cn (G. Huang)
*Corresponding author.

E-mail address: gqhuang@nuaa.edu.cn (G. Huang)

structure and the mechanical response of the joint [10,11]. Nevertheless, the effect of stronger cooling on joint performance is not necessarily determined by the magnitude of grain refinement alone. The NZ, thermo-mechanically affected zone (TMAZ), and base material (BM) undergo different thermomechanical histories and deform together during transverse tensile loading. Their local deformation responses can therefore control the measured strength and ductility of the complete welded specimen [12,13,14].

In the present work, fine-grained NiCoCr MEA plates were welded under air cooling (AFSW) and intensified alcohol–dry ice cooling (LFSW), with the nominal tool rotation and welding speeds held constant. The resulting joints were compared in terms of NZ grain structure, grain-boundary characteristics, BM-to-NZ microstructural transitions, tensile properties, fracture morphology, and digital image correlation (DIC) strain fields. The objective was to clarify the relationship between cooling-dependent grain refinement, joint strengthening, and heterogeneous plastic deformation, and thereby identify the factors governing the strength–ductility response of transverse NiCoCr FSW joints.

2 Experimental procedures

2.1 Material preparation

An approximately 2 kg equiatomic NiCoCr MEA ingot was prepared from high-purity Ni, Co, and Cr by high-frequency vacuum induction melting. The as-cast ingot was homogenized at 1200 °C for 12 h and water cooled, followed by hot forging at 1100 °C. After forging, the alloy was sectioned and machined into rectangular welding plates with a thickness of 3 mm. Before welding, the plates were further processed to obtain the fine-grained initial microstructure characterized in Fig. 1.

2.2 FSW procedure

NiCoCr MEA plates with a thickness of 3 mm were friction stir welded under two cooling conditions: conventional air cooling (AFSW) and intensified cooling using an alcohol–dry ice mixture (LFSW). A W–25 wt.% Re tool was employed, with a shoulder diameter of 15 mm and a tapered probe measuring 2.8 mm in length, 6 mm in root diameter, and 3 mm in tip diameter. For both welding conditions, the tool rotation speed was 500 rpm, the travel speed was 50 mm/min, the plunge depth was 0.2 mm, and the tilt angle was 2°. The welding parameters were kept unchanged to isolate the influence of the external cooling conditions.

During LFSW, the alcohol–dry ice mixture was maintained around the welding region to enhance heat extraction. The advancing side (AS) was defined as the side on which the tangential direction of tool rotation coincided with the welding direction, whereas the retreating side (RS) was defined as the opposite side.

2.3 Microstructure characterization

Cross-sectional specimens were cut perpendicular to the welding direction by electrical discharge machining and mechanically ground and polished. Scanning electron microscopy (SEM) and energy-dispersive X-ray spectroscopy (EDS) were used to examine the microstructure and elemental distribution. Electron backscatter diffraction (EBSD) was employed to characterize grain size, grain-boundary misorientation, and orientation gradients in the BM, TMAZ, and NZ. Low-angle grain boundaries (LAGBs) and high-angle grain boundaries (HAGBs) were defined by misorientations of 2–15° and >15°, respectively. Σ3 twin boundaries were identified from the 60°/<111> relationship with an angular tolerance of 8.66°. Inverse pole figure (IPF), kernel average misorientation (KAM), and grain orientation spread (GOS) maps were used to compare grain structures and local orientation variations [15,16]. KAM was calculated using a 3 × 3 kernel and a maximum neighboring misorientation of 5°; the resulting values were compared as indicators of local lattice-orientation gradients [15,17].

2.4 Mechanical testing

Transverse tensile specimens were machined perpendicular to the welding direction, with the NZ positioned at the center of the gauge section. The specimens had a gauge length of 25 mm, a width of 5 mm, and a thickness of 2.5 mm. Room-temperature tensile tests were conducted at a crosshead speed of 1 mm/min. At least three specimens were tested for each condition. The yield strength (YS), ultimate tensile strength (UTS), and

uniform elongation (UE) were used to evaluate the tensile behavior of the BM and complete transverse welded joints.

DIC was used to characterize the evolution of surface axial strain during tensile loading. A random speckle pattern was applied to the gauge surface, and consecutive images were recorded during the test. The resulting full-field axial-strain maps were examined, and axial-strain profiles were extracted along the A–B measurement line marked in Fig. 9 to compare the spatial strain distributions and localization behavior of the BM, AFSW, and LFSW specimens.

3 Results

3.1 Initial microstructure of the BM

Figure 1 shows the initial microstructure of the NiCoCr BM. The SEM image and corresponding EDS maps (Fig. 1a) reveal an approximately uniform distribution of Ni, Co, and Cr over the observed region. The EBSD IPF map (Fig. 1b) shows a predominantly equiaxed grain structure containing numerous annealing twins, with an average grain size of 18.05 μm. This initial microstructure was used for both welding conditions, allowing the subsequent microstructural differences to be compared on a common basis.

The KAM map (Fig. 1c) is dominated by relatively low local misorientation, with an average KAM of 0.37°. The reported HAGB fraction is 0.94, and the twin-boundary fraction is 0.58. The abundant twins and predominantly low intragranular misorientation characterize the initial BM state before FSW.

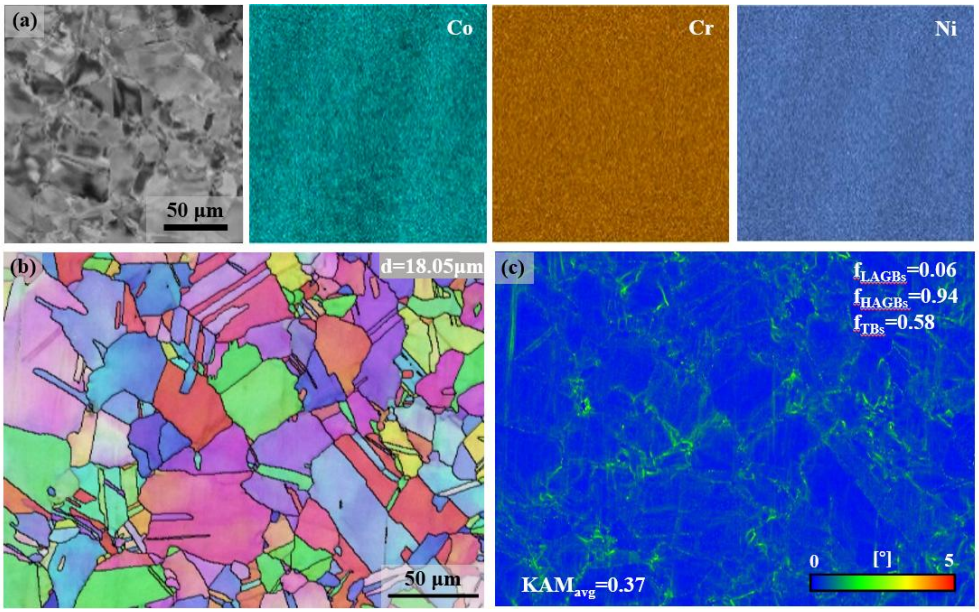


Fig. 1 Initial microstructure of the NiCoCr MEA base material: (a) SEM micrograph and corresponding Co, Cr, and Ni EDS elemental maps; (b) EBSD IPF map; and (c) KAM map. The measured grain size, grain-boundary fractions, and average KAM are indicated in the panels

3.2 Macro- and microstructure of the FSW joints

Figure 2 compares the transverse cross-sectional microstructures of the AFSW and LFSW joints. Both joints exhibit well-formed, basin-shaped NZs without visible macroscopic defects. The AS and RS boundaries are asymmetric, as commonly observed in FSW. Although the overall NZ morphologies are similar, the grain structures differ between the two cooling conditions.

The large-area EBSD IPF maps reveal extensive grain refinement in both NZs compared with the BM. Within each NZ, the grain size varies with position, reflecting the non-uniform deformation and thermal conditions across the welded section [7,18]. The LFSW joint displays a visibly finer grain structure in parts of the NZ, particularly near the outer NZ regions. These observations motivate the position-resolved analysis presented in Fig. 3.

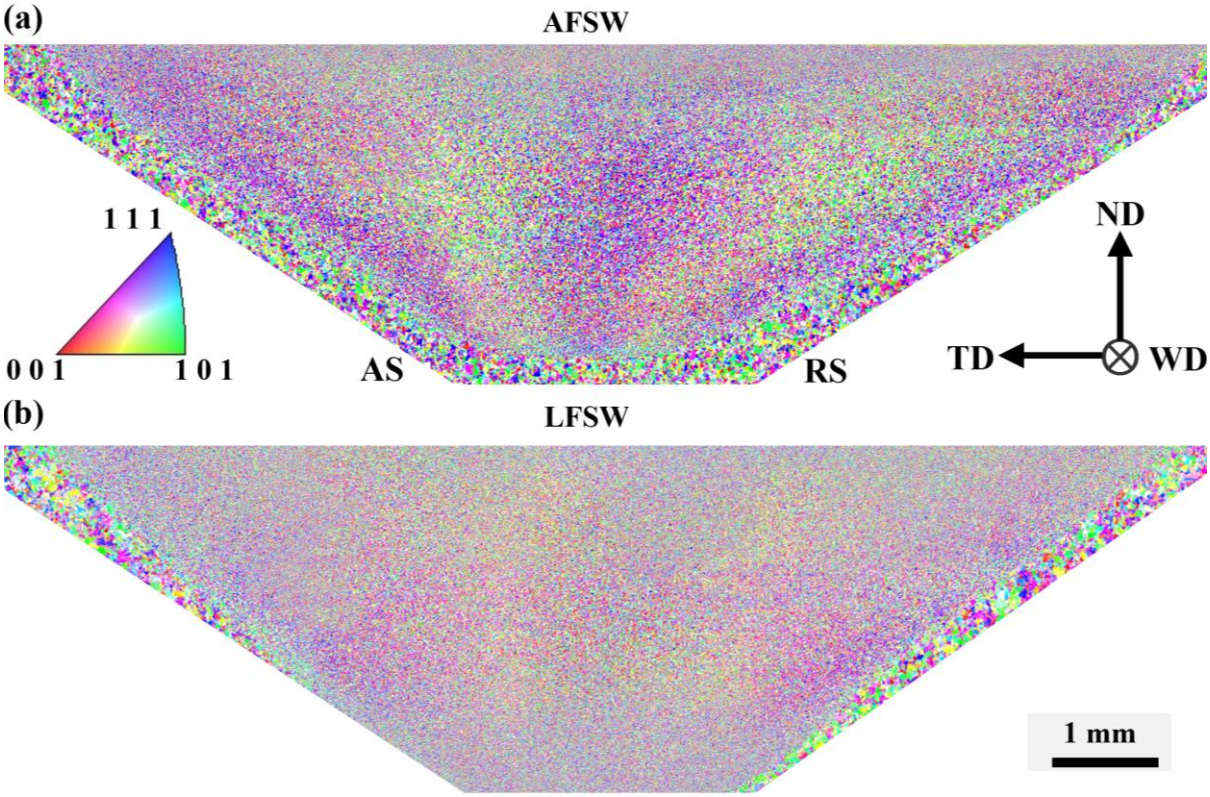


Fig. 2 Cross-sectional EBSD IPF maps of the (a) AFSW and (b) LFSW joints. The shared IPF color key and scale indicate the crystallographic orientations and dimensions; AS and RS denote the advancing and retreating sides, and ND, TD, and WD denote the normal, transverse, and welding directions, respectively

Figure 3 compares the upper and lower NZ grain structures of AFSW (Figs. 3a and 3b) and LFSW (Figs. 3c and 3d). Both joints contain predominantly fine equiaxed grains and abundant twin boundaries. For AFSW, the average grain sizes are 4.85 μm in the upper NZ and 4.77 μm in the lower NZ. The corresponding values decrease to 3.75 and 3.93 μm under LFSW. Thus, the intensified cooling condition reduces the measured grain size by approximately 22.7% and 17.6% in the upper and lower regions, respectively.

Despite the difference in grain size, the boundary-character distributions remain broadly similar. The HAGB fractions in AFSW are approximately 0.94 in both NZ regions, compared with 0.93 and 0.92 in the upper and lower LFSW regions. The corresponding twin-boundary fractions are 0.47 and 0.44 for AFSW and 0.47 and 0.43 for LFSW. Hence, the clearest microstructural distinction between the sampled NZ regions is grain size rather than a major change in the fractions of HAGBs or twin boundaries.

The KAM maps and frequency distributions further reveal relatively low local orientation gradients in both joints (Fig. 3). The average KAM values are 0.41° (upper) and 0.31° (lower) for AFSW, compared with 0.36° (upper) and 0.32° (lower) for LFSW. While there are position-dependent variations, intensified cooling does not produce a systematic increase in the mean KAM. Accordingly, the refinement of the LFSW NZ is accompanied by broadly comparable local misorientation characteristics, rather than by a uniform increase in the measured orientation gradients.

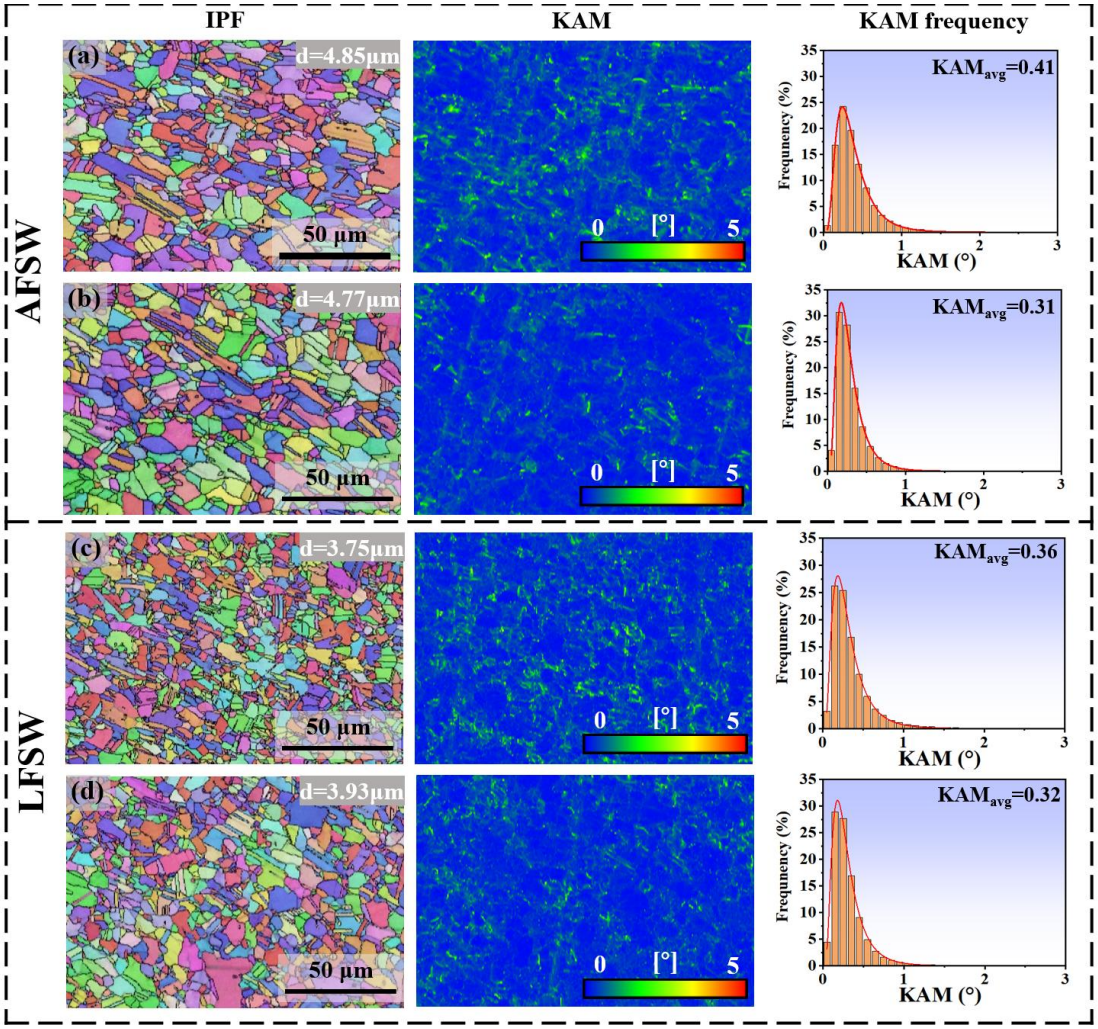


Fig. 3 EBSD characterization of the upper and lower NZ regions in AFSW and LFSW joints: (a) upper AFSW; (b) lower AFSW; (c) upper LFSW; and (d) lower LFSW. Within each row, the IPF map, KAM map, and corresponding KAM frequency distribution are arranged from left to right

Figure 4 presents the grain-structure transitions from the BM toward the NZ on the advancing side of the AFSW (Fig. 4a) and LFSW (Fig. 4b) joints. In both conditions, the IPF maps show a continuous change from relatively large twinned grains outside the NZ to a much finer grain structure in the stirred region. The intermediate zone contains elongated or distorted parent grains together with newly refined grains. Regions I–III marked in the IPF maps capture this progressive microstructural transition and are examined at higher magnification in Figs. 7 and 8.

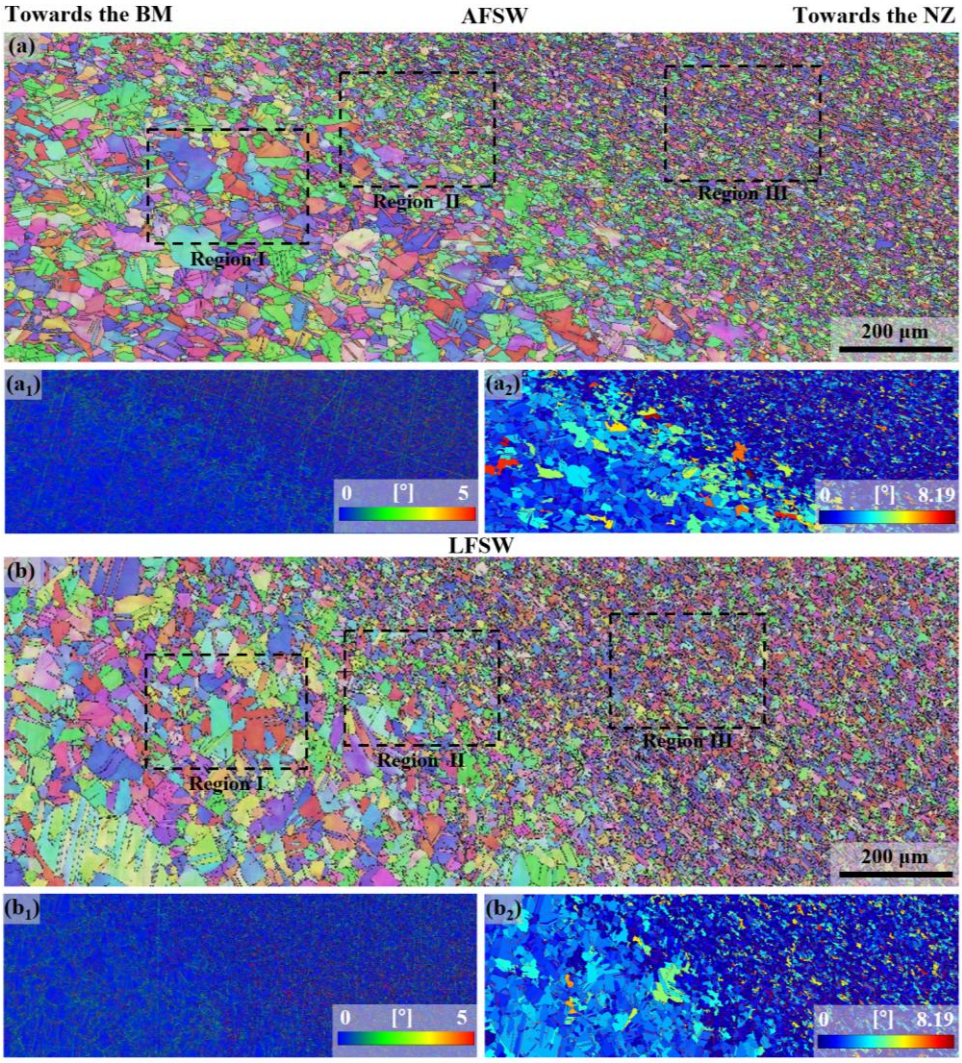


Fig. 4 EBSD characterization of the BM-to-NZ transition on the advancing side: (a, a1, a2) AFSW and (b, b1, b2) LFSW. Panels (a, b) show IPF maps with Regions I–III; (a1, b1) the corresponding KAM maps; and (a2, b2) the GOS maps. Regions I–III are examined in Figs. 7 and 8 for AFSW and LFSW, respectively

The associated KAM and GOS maps reveal a spatial variation in intragranular orientation spread across the transition zone. Local misorientation is particularly evident in deformed grains and near grain boundaries, whereas the fine-grained NZ contains a larger population of grains with relatively low internal orientation spread. The combined IPF, KAM, and GOS observations are consistent with progressive subdivision and recrystallization during FSW [19,20]. The detailed features used to interpret the grain-refinement process are discussed in Section 4.1.

3.3 Mechanical properties

Figure 5a compares the room-temperature engineering stress–strain curves of the BM, AFSW, and LFSW specimens. The BM exhibits a YS of 428 ± 4 MPa, a UTS of 824 ± 6 MPa, and a UE of 64.8 ± 4%. After AFSW, the YS increases to 471 ± 3 MPa and the UTS to 836 ± 4 MPa, while the UE remains high at 62.9 ± 5%. In contrast, LFSW increases the YS further to 546 ± 3 MPa, with a UTS of 828 ± 7 MPa and a UE of 25.0 ± 2%. Relative to AFSW, LFSW therefore raises the YS by 75 MPa (15.9%) but reduces the UE by 37.9 percentage points, while the UTS is essentially unchanged. The two cooling conditions thus lead to different combinations of joint strengthening and uniform plastic deformation.

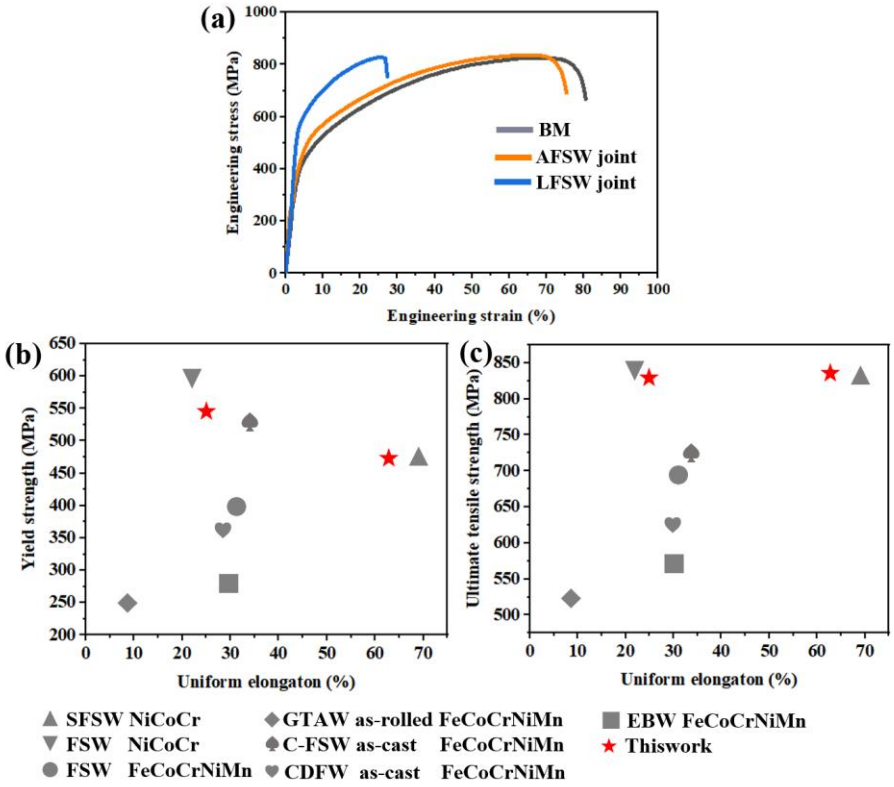


Fig. 5 Room-temperature tensile behavior of NiCoCr BM and transverse FSW joints: (a) engineering stress–strain curves; comparison with reported welded FCC medium/high-entropy alloys in terms of (b) YS–UE and (c) UTS–UE. Red symbols represent the present joints

Figures 5b and 5c compare the YS–UE and UTS–UE combinations of the present joints with published data for welded FCC medium- and high-entropy alloys [8,9,21–23]. Both present joints achieve UTS values above 820 MPa, but their positions on the strength–elongation maps are clearly separated. AFSW combines moderate YS strengthening with the retention of high UE, whereas LFSW reaches a higher YS at considerably lower UE. The contrast demonstrates that the increased resistance to yielding under intensified cooling does not translate into a superior joint-level strength–ductility balance.

Figure 6 compares the tensile fracture morphologies of the BM, AFSW, and LFSW specimens. The low-magnification images (Figs. 6a–c, upper row) show the fracture surfaces of the three specimens. The corresponding high-magnification images in the lower row exhibit dimple-dominated morphologies in all three cases, consistent with ductile fracture by microvoid formation and coalescence. The BM and AFSW specimens show well-developed dimples, whereas LFSW retains a dimpled morphology despite its lower UE. The decreased uniform elongation of LFSW therefore occurs without a corresponding change to a predominantly cleavage-like fracture mode.

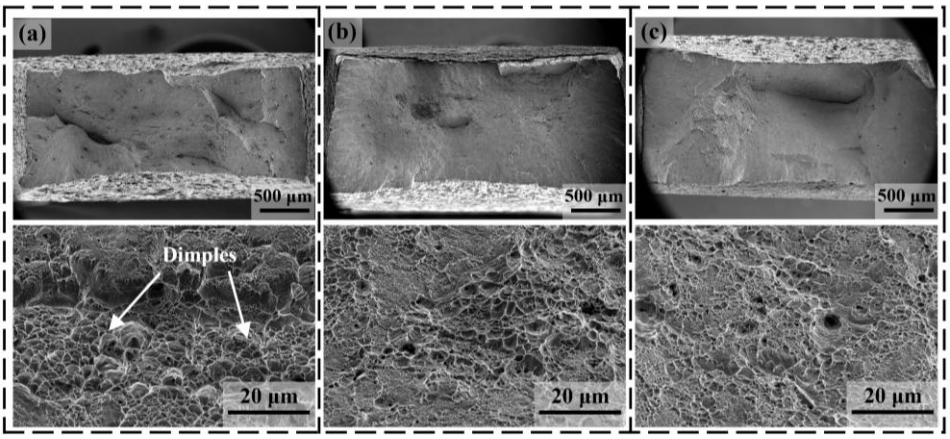


Fig. 6 SEM tensile-fracture morphologies of the BM, AFSW, and LFSW specimens: (a–c) low-magnification fracture surfaces of the BM, AFSW, and LFSW specimens, respectively; the corresponding high-magnification images are arranged directly below the respective panels and show dimpled fracture features

4 Discussion

The cooling-condition comparison reveals two coupled but distinct effects: intensified cooling produces a finer NZ grain structure and a higher transverse-joint yield strength, yet the LFSW joint sustains substantially less uniform deformation than AFSW. Understanding this response requires consideration of both the microstructure formed during welding and the subsequent distribution of plastic strain across the heterogeneous joint.

4.1 Grain refinement and recrystallization across the weld

The region-resolved EBSD maps in Figs. 7 and 8 clarify the microstructural evolution from the BM through the transition region toward the NZ. Although the overall refinement sequences are similar for the two cooling conditions, their final NZ grain sizes differ.

For AFSW (Fig. 7), Region I contains relatively large parent grains with annealing twins and a mean KAM of 0.30°. Region II contains distorted grains, intragranular LAGBs, and small grains distributed along the boundaries of larger grains. The LAGB networks indicate deformation-induced subdivision, a feature associated with continuous dynamic recrystallization (CDRX) [20,24]. The appearance of fine grains near pre-existing boundaries is also consistent with boundary-mediated recrystallization involving discontinuous dynamic recrystallization (DDRX) [19,25]. Toward Region III, fine grains bounded mainly by HAGBs become predominant and the mean KAM reaches 0.41°, illustrating that recrystallization and local orientation gradients coexist within the transition toward the NZ.

The LFSW joint follows a similar sequence (Fig. 8). Region I retains large twinned grains, while Region II exhibits the coexistence of deformed parent grains, subgrain structures, and refined grains near boundaries. Region III is dominated by finer grains. The mean KAM values increase from 0.30° in Region I to 0.34° and 0.39° in Regions II and III, respectively. Taken together, the observed boundary-associated refinement and intragranular subdivision suggest contributions from both DDRX-like boundary processes and CDRX-like subgrain evolution in the two joints. At the same nominal welding parameters, the additional external cooling in LFSW is associated with smaller final NZ grains. This is consistent with stronger thermal extraction restricting the extent of grain growth during and after dynamic recrystallization [7,10,11]. The limited changes in HAGB, twin-boundary, and KAM statistics suggest that cooling principally modifies the retained grain scale rather than producing a fundamentally different boundary-character distribution.

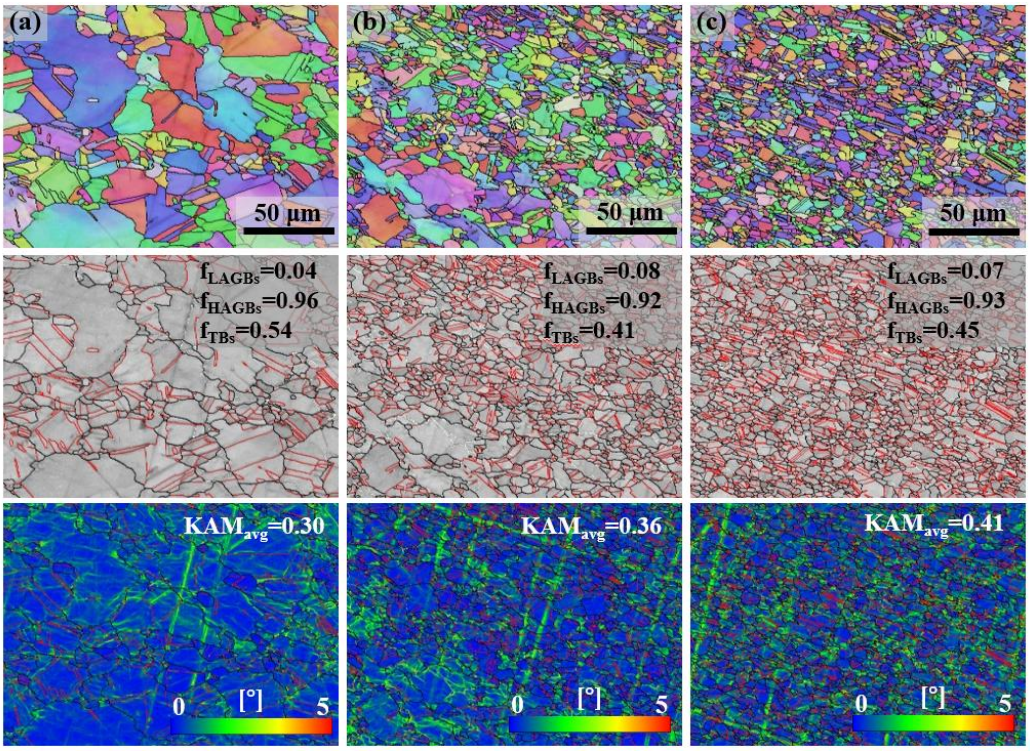


Fig. 7 Detailed EBSD characterization of AFSW Regions I-III marked in the IPF map of Fig. 4a: (a–c) IPF maps of Regions I–III, respectively; the middle and bottom rows show the corresponding grain-boundary and KAM maps in the same left-to-right order. Black, white, and red lines denote HAGBs, LAGBs, and Σ3 twin boundaries, respectively

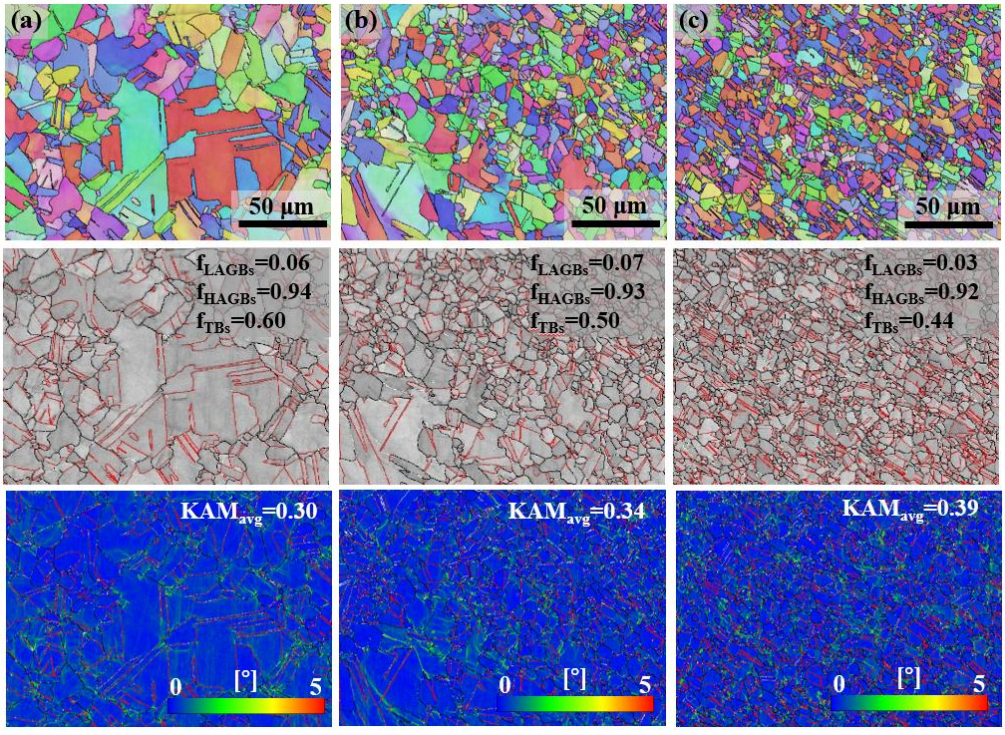


Fig. 8 Detailed EBSD characterization of LFSW Regions I-III marked in the IPF map of Fig. 4b: (a–c) IPF maps of Regions I–III, respectively; the middle and bottom rows show the corresponding grain-boundary and KAM maps in the same left-to-right order. Black, white, and red lines denote HAGBs, LAGBs, and Σ3 twin boundaries, respectively

4.2 Tensile response and heterogeneous strain partitioning

The grain refinement in LFSW provides a plausible structural basis for its increased resistance to yielding. In FCC alloys, smaller grains increase the frequency of grain-boundary obstacles to slip, and grain-boundary

strengthening has been demonstrated in CrCoNi alloys [3,4]. The measured upper and lower NZ grain sizes are both smaller in LFSW than in AFSW (Fig. 3). However, transverse tensile specimens include the NZ, TMAZ, and BM within the same gauge section; their strength and elongation therefore reflect the combined response of regions with different local microstructures. In particular, a higher resistance to plastic flow in the NZ does not require all regions of the joint to deform uniformly.

The engineering stress–strain responses reveal the resulting difference in plastic deformation capacity (Fig. 5a). AFSW increases the YS from 428 MPa for the BM to 471 MPa while retaining nearly the same UE (62.9% versus 64.8%). LFSW increases the YS further to 546 MPa, but its UE falls to 25.0%, despite a comparable UTS. The corresponding differences between UTS and YS are 365 MPa for AFSW and 282 MPa for LFSW, consistent with a shorter uniform-deformation stage in the latter condition. Thus, grain refinement under intensified cooling improves the initial resistance to yielding, while the overall tensile response reflects an increasing competition between local strengthening and the ability of the surrounding regions to accommodate strain.

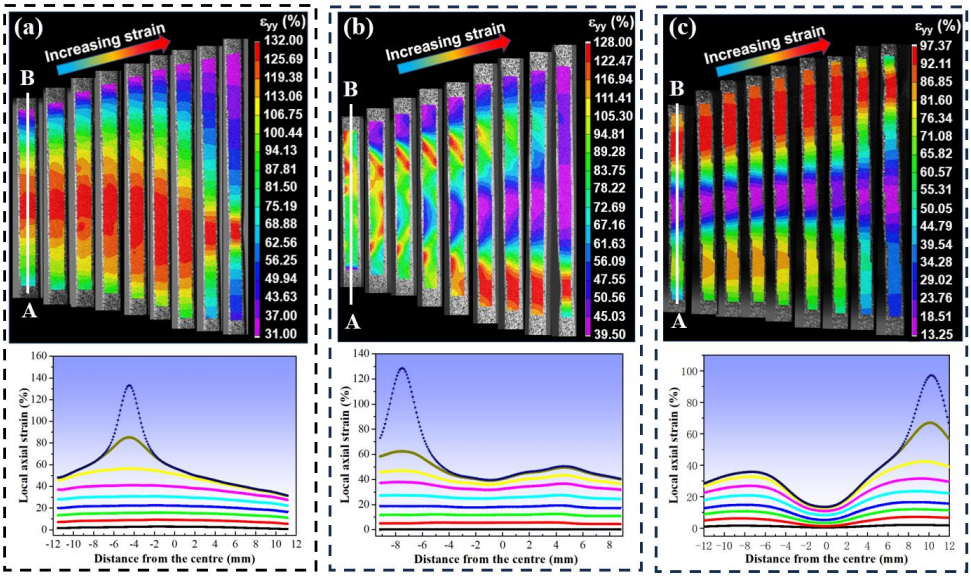


Fig. 9 Evolution of the axial-strain fields and corresponding line profiles obtained by DIC for (a) BM, (b) AFSW, and (c) LFSW during room-temperature tensile testing. For each specimen, sequential full-field axial-strain maps are shown above the corresponding strain profiles along the marked A–B line. The arrows indicate increasing tensile strain

Figure 9 provides direct evidence of this heterogeneous deformation response. In the BM specimen (Fig. 9a), strain becomes concentrated in a localized region as tensile loading proceeds. In both welded specimens (Figs. 9b and 9c), the central NZ exhibits relatively low axial strain, while larger strains develop in neighboring regions. The accompanying line profiles make the non-uniform strain distribution particularly clear. The LFSW profiles show a stronger separation between the low-strain central region and the more highly strained surrounding material, whereas strain in AFSW is distributed more broadly during tensile loading. These features agree with the distinct UE values and identify strain partitioning across the joint as an important factor governing the macroscopic response.

The observed strain fields can be understood in terms of deformation compatibility between neighboring regions. A fine-grained NZ offers greater resistance to plastic deformation than the adjacent, more compliant regions, so transverse tensile loading produces non-uniform plastic strain across the joint. Differences in local flow resistance can also generate strain gradients near the interfaces between regions and influence the evolution of the internal stress state [12,26,27]. Such interactions are central to the mechanical behavior of heterogeneous metals [28,29]. In the present joints, however, a favorable outcome depends on whether the surrounding regions can continue to accommodate strain without excessive concentration. AFSW retains more distributed plastic deformation and a high UE, whereas the larger strain contrast observed in LFSW is accompanied by a pronounced reduction in UE.

This distinction is consistent with previous studies showing that heterogeneous microstructures can combine strength and ductility when their hard and compliant regions deform cooperatively [29,30]. In a welded joint, the constituent regions are arranged spatially across the tensile gauge length rather than being uniformly intermixed. Consequently, strengthening the NZ alone can increase the difference in plastic response between the weld center and its surroundings. The present comparison indicates that the additional NZ refinement achieved by LFSW strengthens the joint at yielding but concentrates a larger share of the subsequent plastic deformation outside the NZ. The dimpled fracture surfaces in both welding conditions (Fig. 6) further support a ductile fracture response, while the reduction in uniform elongation is associated with the distribution and concentration of plastic strain rather than an abrupt transition to brittle fracture.

Taken together, the EBSD, tensile, fracture, and DIC results establish a coherent relationship between the cooling strategy and joint performance. Intensified cooling favors a finer retained NZ grain structure, which contributes to higher yielding resistance. At the same time, the transverse joint must accommodate deformation across the NZ–TMAZ–BM microstructural gradient. The improved NZ strengthening in LFSW is therefore accompanied by stronger strain partitioning and reduced uniform elongation. The comparison shows that effective thermal management in FSW should be evaluated through both microstructural refinement and deformation compatibility at the joint scale.

5 Conclusions

This study compared the microstructural evolution and tensile behavior of fine-grained NiCoCr MEA joints produced by air-cooled and alcohol–dry ice-assisted FSW at identical nominal welding parameters. The principal conclusions are as follows:

(1) Both AFSW and LFSW produced sound joints with refined, predominantly equiaxed NZ grains. EBSD revealed a gradual BM–TMAZ–NZ transition involving intragranular subgrain formation and boundary-associated grain refinement, consistent with contributions from continuous and discontinuous dynamic recrystallization processes.

(2) Intensified cooling further refined the NZ. The average upper and lower NZ grain sizes decreased from 4.85 and 4.77 μm in AFSW to 3.75 and 3.93 μm in LFSW, respectively. HAGB and twin-boundary fractions remained broadly comparable, while the mean KAM values showed no systematic increase under LFSW.

(3) AFSW produced a YS of 471 ± 3 MPa, a UTS of 836 ± 4 MPa, and a UE of 62.9 ± 5%. LFSW increased the YS to 546 ± 3 MPa, while maintaining a similar UTS (828 ± 7 MPa); however, the UE decreased to 25.0 ± 2%. Therefore, the additional strengthening from LFSW was accompanied by a marked loss of uniform deformation capacity.

(4) DIC showed preferential plastic deformation outside the refined NZ in both joints and more pronounced spatial strain partitioning under LFSW. The results demonstrate that the tensile performance of NiCoCr FSW joints depends on the balance between NZ strengthening and deformation compatibility across the entire transverse joint.

Statements and Declarations

Funding

G.Q. Huang gratefully acknowledges the financial support from the National Natural Science Foundation of China (Grant No. 52205436) and the Fundamental Research Funds for the Central Universities (Grant No. NS2025018).

Competing interests

The authors declare that they have no competing interests.

Data availability

The datasets generated and analyzed during the current study are available from the corresponding author upon reasonable request.

Author contributions

Borui Zhang: Writing – original draft, Visualization, Methodology, Investigation, Formal analysis, Data curation, Conceptualization. **Jinpeng Hu:** Investigation, Data curation. **Yifu Shen:** Writing – review & editing, Validation, Resources, Formal analysis. **Zhikang Shen:** Investigation, Data curation. **Tzuhsiu Chou:** Writing – review & editing, Validation, Formal analysis. **Guoqiang Huang:** Writing – review & editing, Supervision, Resources, Project administration, Funding acquisition, Conceptualization.

References

1. George EP, Curtin WA, Tasan CC (2020) High entropy alloys: A focused review of mechanical properties and deformation mechanisms. Acta Mater 188:435–474. https://doi.org/10.1016/j.actamat.2019.12.015

2. Liu D, Yu Q, Kabra S, Jiang M, Forna-Kreutzer P, Zhang R, Payne M, Walsh F, Gludovatz B, Asta M, Minor AM, George EP, Ritchie RO (2022) Exceptional fracture toughness of CrCoNi-based medium- and high-entropy alloys at 20 kelvin. Science 378:978–983. https://doi.org/10.1126/science.abp8070

3. Yoshida S, Bhattacharjee T, Bai Y, Tsuji N (2017) Friction stress and Hall-Petch relationship in CoCrNi equi-atomic medium entropy alloy processed by severe plastic deformation and subsequent annealing. Scr Mater 134:33–36. https://doi.org/10.1016/j.scriptamat.2017.02.042

4. Schneider M, George EP, Manescau TJ, Záležák T, Hunfeld J, Dlouhý A, Eggeler G, Laplanche G (2020) Analysis of strengthening due to grain boundaries and annealing twin boundaries in the CrCoNi medium-entropy alloy. Int J Plast 124:155–169. https://doi.org/10.1016/j.ijplas.2019.08.009

5. Zhu Z, Yan S, Chen H, Gou G (2021) Unprecedented combination of strength and ductility in laser welded NiCoCr medium entropy alloy joints. Mater Sci Eng A 803:140501. https://doi.org/10.1016/j.msea.2020.140501

6. Mishra RS, Ma ZY (2005) Friction stir welding and processing. Mater Sci Eng R Rep 50:1–78. https://doi.org/10.1016/j.mser.2005.07.001

7. Heidarzadeh A, Mironov S, Kaibyshev R, Çam G, Simar A, Gerlich A, Khodabakhshi F, Mostafaei A, Field DP, Robson JD, Deschamps A, Withers PJ (2021) Friction stir welding/processing of metals and alloys: a comprehensive review on microstructural evolution. Prog Mater Sci 117:100752. https://doi.org/10.1016/j.pmatsci.2020.100752

8. Hu Y, Niu Y, Zhao Y, Yang W, Ma X, Li J (2022) Friction stir welding of CoCrNi medium-entropy alloy: Recrystallization behaviour and strengthening mechanism. Mater Sci Eng A 848:143361. https://doi.org/10.1016/j.msea.2022.143361

9. Huang GQ, Chou TH, Liu SF, Xiao B, Ju J, Gan J, Yang T, Zhang P, Yang JX, Lu CY, Meng FQ (2023) Unveiling the microstructure evolution and mechanical properties of submerged friction stir welded joint of fine-grained NiCoCr medium entropy alloy. Mater Charact 200:112903. https://doi.org/10.1016/j.matchar.2023.112903

10. Cao F, Sun T, Hu J, Hou W, Huang G, Shen Y, Ma N, Geng P, Hu W, Qu X (2023) Enhanced mechanical and anticorrosion properties in cryogenic friction stir processed duplex stainless steel. Mater Des 225:111492. https://doi.org/10.1016/j.matdes.2022.111492

11. Akbari M, Kazemi MA, Moghanian A, Hassanzadeh E (2026) Thermal management in friction stir welding: A review of cooling and heat-assisted techniques. Mater Today Commun 53:115419. https://doi.org/10.1016/j.mtcomm.2026.115419

12. Zhu Y, Wu X (2023) Heterostructured materials. Prog Mater Sci 131:101019. https://doi.org/10.1016/j.pmatsci.2022.101019

13. Vysotskii I, Malopheyev S, Mironov S, Kaibyshev R (2022) Deformation behavior of friction-stir welded Al-Mg-Mn alloy with ultrafine-grained structure. Mater Charact 185:111758. https://doi.org/10.1016/j.matchar.2022.111758

14. Suthar H, Bhattacharya A, Paul SK (2022) Characterizing the anisotropic response of similar and dissimilar FSW joints by DIC-based simultaneous strain measurements on two orthogonal surfaces. J Manuf Process 84:697–712. https://doi.org/10.1016/j.jmapro.2022.10.036

15. Wright SI, Nowell MM, Field DP (2011) A review of strain analysis using electron backscatter diffraction. Microsc Microanal 17:316–329. https://doi.org/10.1017/S1431927611000055

16. Mitsche S, Poelt P, Sommitsch C (2007) Recrystallization behaviour of the nickel-based alloy 80A during hot forming. J Microsc 227:267–274. https://doi.org/10.1111/j.1365-2818.2007.01810.x

17. Pantleon W (2008) Resolving the geometrically necessary dislocation content by conventional electron backscattering diffraction. Scr Mater 58:994–997. https://doi.org/10.1016/j.scriptamat.2008.01.050

18. Cao F, Huang G, Guan W, Hou W, Ni R, Shen Y, Liu Q (2022) Inhomogeneous microstructure and properties along the thickness of stir zone in friction stir welded SAF 2507 super duplex stainless steel joint. J Manuf Process 73:611–623. https://doi.org/10.1016/j.jmapro.2021.11.043

19. Mironov S, Sato YS, Kokawa H, Inoue H, Tsuge S (2011) Structural response of superaustenitic stainless steel to friction stir welding. Acta Mater 59:5472–5481. https://doi.org/10.1016/j.actamat.2011.05.021

20. Sakai T, Belyakov A, Kaibyshev R, Miura H, Jonas JJ (2014) Dynamic and post-dynamic recrystallization under hot, cold and severe plastic deformation conditions. Prog Mater Sci 60:130–207. https://doi.org/10.1016/j.pmatsci.2013.09.002

21. Wu ZG, David SA, Feng ZL, Bei H (2016) Weldability of a high entropy CrMnFeCoNi alloy. Scr Mater 124:81–85. https://doi.org/10.1016/j.scriptamat.2016.06.046

22. Oliveira JP, Curado TM, Zeng Z, Lopes JG, Rossinyol E, Park JM, Schell N, Braz Fernandes FM, Kim HS (2020) Gas tungsten arc welding of as-rolled CrMnFeCoNi high entropy alloy. Mater Des 189:108505. https://doi.org/10.1016/j.matdes.2020.108505

23. Shaysultanov D, Stepanov N, Malopheyev S, Vysotskiy I, Sanin V, Mironov S, Kaibyshev R, Salishchev G, Zherebtsov S (2018) Friction stir welding of a carbon-doped CoCrFeNiMn high-entropy alloy. Mater Charact 145:353–361. https://doi.org/10.1016/j.matchar.2018.08.063

24. Gourdet S, Montheillet F (2003) A model of continuous dynamic recrystallization. Acta Mater 51:2685–2699. https://doi.org/10.1016/S1359-6454(03)00078-8

25. Jeon JJ, Mironov S, Sato YS, Kokawa H, Park SHC, Hirano S (2013) Grain structure development during friction stir welding of single-crystal austenitic stainless steel. Metall Mater Trans A 44:3157–3166. https://doi.org/10.1007/s11661-013-1692-0

26. Yang M, Pan Y, Yuan F, Zhu Y, Wu X (2016) Back stress strengthening and strain hardening in gradient structure. Mater Res Lett 4:145–151. https://doi.org/10.1080/21663831.2016.1153004

27. Huang CX, Wang YF, Ma XL, Yin S, Höppel HW, Göken M, Wu XL, Gao HJ, Zhu YT (2018) Interface affected zone for optimal strength and ductility in heterogeneous laminate. Mater Today 21:713–719. https://doi.org/10.1016/j.mattod.2018.03.006

28. Wu X, Zhu Y (2017) Heterogeneous materials: a new class of materials with unprecedented mechanical properties. Mater Res Lett 5:527–532. https://doi.org/10.1080/21663831.2017.1343208

29. Ma E, Wu X (2019) Tailoring heterogeneities in high-entropy alloys to promote strength–ductility synergy. Nat Commun 10:5623. https://doi.org/10.1038/s41467-019-13311-1

30. Lin PT, Liu HC, Hsieh PY, Wei CY, Tsai CW, Sato YS, Chen SC, Yen HW, Lu NH, Chen CH (2021) Heterogeneous structure-induced strength-ductility synergy by partial recrystallization during friction stir welding of a high-entropy alloy. Mater Des 197:109238. https://doi.org/10.1016/j.matdes.2020.109238